Banner appropriate to article type will appear here in typeset article

Locomotion with a wavy cylindrical filament in a yield-stress fluid

D. R. Hewitt[1] & N. J. Balmforth[2]

[1]Department of Mathematics, University College, London, WC1H 0AY, UK

[2]Department of Mathematics, University of British Columbia, Vancouver, BC, V6T 1Z2, Canada

(Received xx; revised xx; accepted xx)

A yield stress is added to Taylor's (1952, *Proc. Royal Soc. A*, **211**, 225-239) model of a microscopic organism with a wavy cylindrical tail swimming through a viscous fluid. Viscoplastic slender-body theory is employed for the task, generalizing existing results for Bingham fluid to the Herschel-Bulkley constitutive model. Numerical solutions are provided over a range of the two key parameters of the problem: the wave amplitude relative to the wavelength, and a Bingham number which describes the strength of the yield stress. Numerical solutions are supplemented with discussions of various limits of the problem in which analytical progress is possible. If the wave amplitude is sufficiently small, the yield stress of the material inevitably dominates the flow; the resulting 'plastic locomotion' results in swimming speeds that depend strongly on the swimming gait, and can, in some cases, even be negative. Conversely, when the yield stress is large, swimming becomes possible at the wave speed, with the swimmer sliding or burrowing along its centreline.

1. Introduction

The fluid mechanics of locomotion through viscous fluids was pioneered by Taylor and Lighthill over half a century ago. Taylor's (1952) model of locomotion driven by the waving of a cylindrical filament, in particular, lay the foundation for biofluid mechanics of flagellar motion. Taylor's theory applied for low-amplitude motions, such that the swimming stroke constituted a small perturbation of the boundary corresponding to the swimmer's surface. Later developments by Hancock (1953) and Lighthill (1975) exploited the machinery of Stokes flow theory to advance beyond this regime. Lauga & Powers (2009) provide a review of later developments.

More recently it has become popular to consider locomotion through complex fluids, motivated mostly by the settings of many problems in physiology and the environment. Viscoelastic fluid models have been the most popular idealization used in theoretical and experimental explorations to date. However, locomotion through or above viscoplastic fluids (Denny 1980, 1981; Chan *et al.* 2005; Pegler & Balmforth 2013; Hewitt & Balmforth 2017, 2018; Supekar *et al.* 2020) and both wet and dry granular media (Hosoi & Goldman 2015; Maladen *et al.* 2009; Jung

2010; Juarez *et al.* 2010; Dorgan *et al.* 2013; Kudrolli & Ramirez 2019) have also been of interest.

For waving cylindrical filaments in viscous fluid, an awkward drawback in theoretical explorations is that long-range effects characteristic of Stokes flow plague analytical advances even when the filament is relatively thin (Cox 1970; Keller & Rubinow 1976; Lighthill 1975; Lauga & Powers 2009). In particular, Lighthill's resistive force theory, the simplest theory based on the slenderness of the filament, converges only logarithmically in terms of aspect ration. By contrast, the localization of flow around the filament by a yield stress ensures that the viscoplastic analogue of this theory is more accurate than its Newtonian cousin, as also noted in the context of granular media (Zhang & Goldman 2014; Hosoi & Goldman 2015). We exploited this feature in a previous article (Hewitt & Balmforth (2018)) to develop viscoplastic slender-body theory. We further applied the theory to models of swimming driven by the motion of a helical filament (a model also popularized by Taylor and Hancock).

In the current theory we use the viscoplastic slender-body theory to attack Taylor's problem of locomotion by a wavy cylindrical filament. For this task, we first generalize our previous results by considering the ambient fluid to be described by the Herschel-Bulkley model. In our previous work (Hewitt & Balmforth 2018), we considered only the Bingham model, for which the plastic viscosity beyond the yield point is constant. Most real materials, however, possess a nonlinear (and typically shear-thinning) viscosity, leading us to use the Herschel-Bulkley model (even though the behaviour of those materials is invariably richer than this idealization; Balmforth *et al.* (2014)). Discussions of the effect of shear thinning on locomotion have appeared previously (*e.g.* (Vélez-Cordero & Lauga 2013; Li & Ardekani 2015; Riley & Lauga 2017)), although these have mostly focussed on power-law fluids and the like, whereas our main thrust is to understand the impact of a yield stress. From the perspective of complex fluids, the inclusion of a yield stress is typically dramatic, qualitatively changing the dynamics, and permits one to access the "plastic limit" where the medium behaves more like a perfectly plastic, cohesive solid (Prager & Hodge 1951).

A notable detail of the current problem is that one might expect that the localization of flow by the yield stress should continue all the way to the plastic limit, thereby restricting motion to narrow boundary layers around the swimmer (Balmforth *et al.* 2017). However, it turns out that this only becomes true when the filament can translate nearly along its length. Otherwise, regions of almost perfectly plastic deformation persists over distances of order the radius driven by transverse motion. The transverse and axial forces acting on the filament are then of similar size, unless the motion is closely aligned with its axis. We explored some consequences of the strong force anisotropy that is experienced only in nearly axial motion in Hewitt & Balmforth (2018) for some other problems of viscoplastic flows around slender filaments. Here, we examine the possibility whether it can lead to style of locomotion in which in which the swimmer "burrows" through the fluid, moving purely in the direction of its centreline. Such a style of motion is, in fact, often observed for real organisms (Gidmark *et al.* 2011; Dorgan *et al.* 2013; Kudrolli & Ramirez 2019).

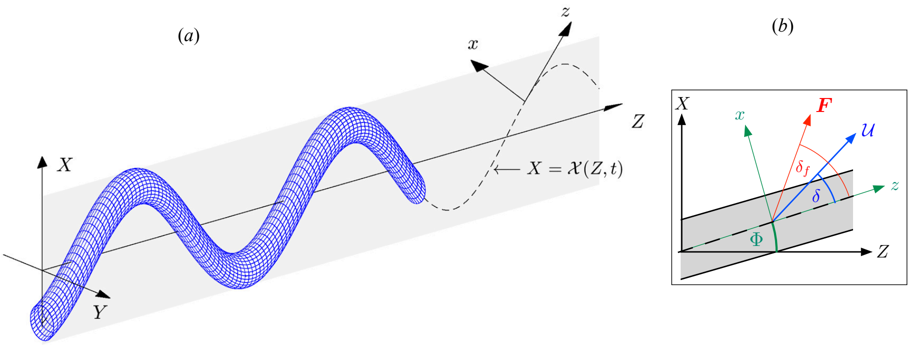

Figure 1: Sketches of (a) the swimmer geometry, and (b) the local coordinates (x, z) aligned with a segment of the cylindrical body that lies at an angle $\Phi(Z)$ to the Z axis. The segment moves with speed $\mathcal{U}$ at a direction δ to its axis; the associated force $\boldsymbol{F}$ is directed at an angle δ_f to its axis.

2. Formulation

Consider a cylindrical filament of radius $\mathcal{R}$ moving without inertia through a viscoplastic fluid described by the Herschel-Bulkley constitutive law, with yield stress $\tau_{_Y}$, consistency K and power-law index n. The filament is propelled by waves generated along its length, with wavepeed c and wavelength λ. A sketch of the geometry is shown in figure 1; the waves are assumed to deform the filament in the $(X, Z)-$plane, with the $Z-$axis pointing in the direction of motion. The instantaneous centreline of the filament is given by the curve $X = \mathcal{X}(Z + ct)$, which we assume is inextensible. As a canonical example, we follow Taylor and consider the sinusoidal waveform,

$$X = \mathcal{X}(Z + ct) = a\lambda \sin\left[\frac{2\pi(Z + ct)}{\lambda}\right], \qquad (2.1)$$

with (dimensionless) peak amplitude a. In fact, we also open up the possibility of locomotion driven by more general waveforms, although we restrict attention to cases that are symmetric with $\mathcal{X}(Z) = -\mathcal{X}(-Z)$ and $\mathcal{X}(Z) = \mathcal{X}(\frac{1}{4}\lambda - Z)$ (for $0 < X < \frac{1}{2}\lambda$), such that the waveform has the extrema $\mathcal{X}(\pm\frac{1}{4}\lambda) = \pm a$ and zeros $\mathcal{X}(0) = \mathcal{X}(\pm\frac{1}{2}\lambda) = 0$.

2.1. *Viscoplastic slender-body theory*

When the filament is long and thin, the localization of motion by the yield stress implies that the flow is locally equivalent to that around a straight cylinder. This approximation is expected to remain accurate as long as variations along the axis of the filament are much smaller that the radius (so $\mathcal{R} \ll \lambda$), and the yield stress is sufficiently large that the fluid plugs up beyond a distance of order the filament radius (that is, the Bingham number, to be defined presently, is order unity or larger).

In this situation, the inertia-free problem breaks down into the computation of the force generated locally by the translation of the cylinder with respect to the fluid. The ensuing fluid motion is most naturally described in terms of a local $(x, z)-$coordinate system attached to the centerline of the filament, with z pointing along the length (see figure 1). If the cylinder translates with velocity $\mathcal{U}(\hat{\mathbf{x}} \sin\delta + \hat{\mathbf{z}} \cos\delta)$ at an angle δ to its axis (figure 1b), the resulting force per unit length can be represented as

$$\frac{K\mathcal{U}^n}{\mathcal{R}^{n-1}}\left[\hat{\mathbf{x}}F_x(\delta,n,Bi)+\hat{\mathbf{z}}F_z(\delta,n,Bi)\right], \tag{2.2}$$

where the local Bingham number, which measures the relative importance of the yield stress and the characteristic viscous stresses, is

$$Bi=\frac{\tau_{_Y}\mathcal{R}^n}{K\mathcal{U}^n}, \tag{2.3}$$

and $\hat{\mathbf{x}}$ and $\hat{\mathbf{z}}$ denote unit vectors in the local x and z directions, respectively. A fuller statement of the problem can be found in Appendix A.1.

The nonlinearity of the constitutive law forbids any simple breakdown of the dependence of the force components F_x and F_z on the angle δ and Bi, although analytical results are available in certain limits (see Hewitt & Balmforth (2018)). The key to solving the locomotion problem more generally, however, is to tabulate these components for a given n, and then use an interpolation to integrate over the length of the wavy filament, accounting for the relevant orientation of each local cylindrical cross-section.

Before performing this operation, we briefly revisit and generalise the results reported by Hewitt & Balmforth (2018). In that paper, force components (F_x, F_z) were computed numerically over a wide range of values for Bi and δ (there written alternatively in terms of an angle $\phi\equiv\frac{1}{2}\pi-\delta$) for a Bingham fluid ($n=1$). We repeat this exercise here, but for more values of n, using a simple adaptation of the numerical scheme in Hewitt & Balmforth (2018) (see Appendix A.1). Figure 2(a,b) shows how the force direction, $\delta_f=\tan^{-1}(F_z/F_x)$, and magnitude, $F\equiv\sqrt{F_x^2+F_z^2}$, vary with δ and Bi for three values of n. The main variation of the force magnitude is with Bi; to extract this dominant dependence, the plots show $F/\langle F\rangle$, where $\langle F\rangle$ denotes the average over $0\leqslant\delta\leqslant\frac{1}{2}\pi$, which reduces the variation to a factor of about three. The angular averages themselves are also shown against Bi in figure 2(c).

Considering first the case of low Bingham number, $Bi\ll 1$, one might expect that the force components converge to those for a power-law fluid. However, for the Newtonian case, the Stokes paradox ensures that the low deformation rates in the far-field always impact the result. This leads to a persistent, logarithmic dependence on Bi that reflects how the yield stress must inevitably bring fluid to rest and resolve the paradox. Explicitly (for $n=1$), we have

$$(F_x,F_z)\to-\frac{2\pi}{\log Bi^{-1}}(2\sin\delta,\cos\delta), \tag{2.4}$$

as $Bi\to 0$ (Hewitt & Balmforth 2018). On the other hand, shear-thinning avoids the Stokes paradox for $n<1$, as pointed out by Tanner (1993), leading to a finite drag force for $Bi\to 0$, as illustrated in figure 2(c). While there is no general analytic solution for arbitrary δ in this limit, an exact solution can be computed for pure axial motion,

$$F_z(\tfrac{1}{2}\pi,n,0)=2\pi(n^{-1}-1)^n, \tag{2.5}$$

if $n<1$. The convergence of the drag components to their power-law limits for $n=\frac{1}{2}$ and $Bi\ll 1$ is illustrated further in figure 2(d). This plot shows $|F_x|/\sin\delta$ and $|F_z|/\cos\delta$; this scaling, motivated by the form of the Newtonian limit (2.4), takes care of most of the δ-dependence of F_z, but works less well for

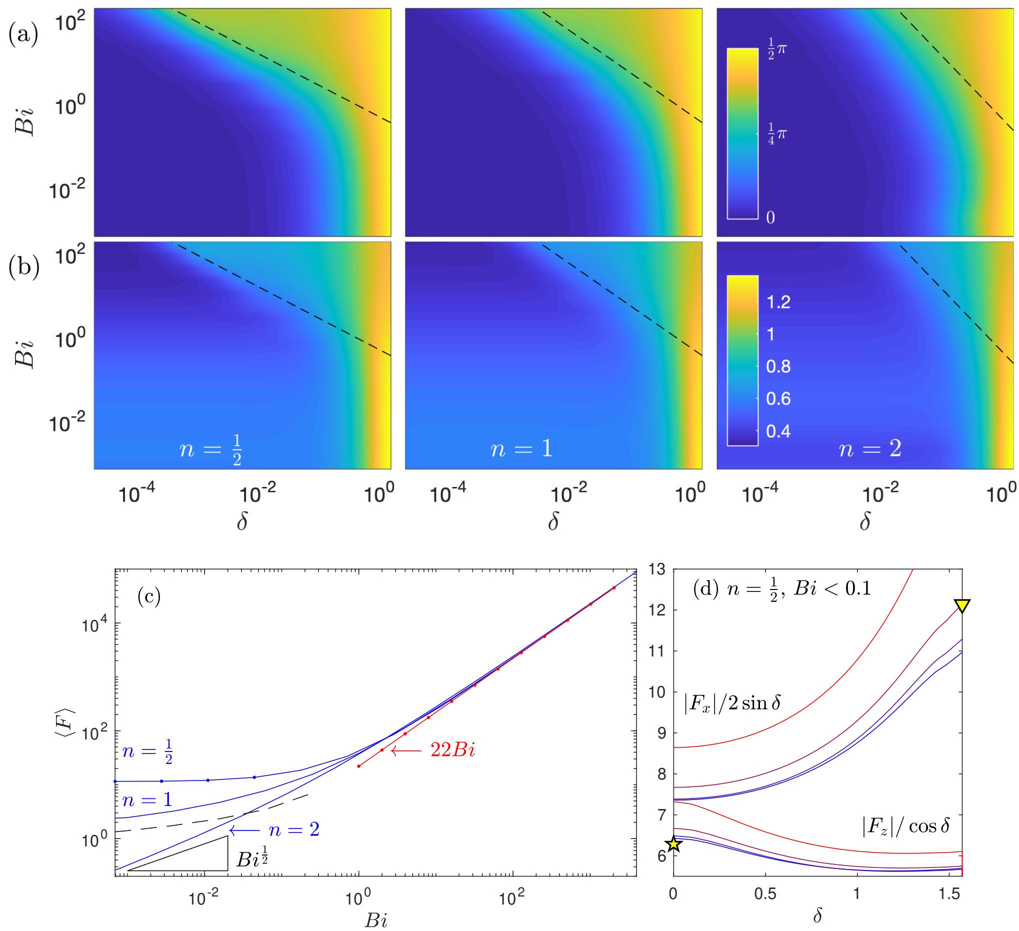

Figure 2: Slender-body-theory results for motion of a cylinder in a Herschel–Bulkley fluid with index n. Colour maps of (a) force direction δ_f and (b) $F/\langle F\rangle$, for $n = 0.5$ (left), $n = 1$ (centre) and $n = 2$ (right), where $F = \sqrt{F_x^2 + F_z^2}$ and $\langle F\rangle$ is the angular average shown in (c). The dashed lines in (a)-(b) show $\delta = (\beta/\alpha_n)Bi^{-2/(1+n)}$, where α_n is defined in (2.7), and that in (c) shows (2.4). Panel (d) plots the scaled force components $|F_x|/\sin\delta$ and $|F_z|/\cos\delta$, for $n = \frac{1}{2}$ and $Bi = 4^{-j}$ with $j = 2$, 3, 4, 5 (as indicated by the blue dots in (c), with colours from red at $Bi = 4^{-2}$ to blue at $Bi = 4^{-5}$); the star shows the analytical result in (2.5), and the triangle indicates an approximate solution from Tanner (1993) ($F_x \approx 12.1$).

F_x. Thus, an empirical collapse of the form suggested by Chhabra *et al.* (2001) for Carreau fluids (and which was exploited for locomotion problems by Riley & Lauga (2017)), which implies $F_x(\delta, n, 0)/F_z(\delta, n, 0) = F_x(\delta, 1, 0)/F_z(\delta, 1, 0) = 2\tan\delta$, does not apply accurately in this power-law limit.

For $n > 1$, the Stokes paradox persists and the drag again vanishes in the limit $Bi \to 0$. In this case, the far-field solution for the streamfunction in the cross-sectional plane is expected to contain terms of the form $\psi \sim Cr^{2-\frac{1}{n}}\sin\theta$ (see Tanner (1993)). Demanding that such terms balance the term stemming from sideways translation $\psi \propto r\sin\theta$ for $r = O(Bi^{-1})$ suggests that $C = O(Bi^{1-\frac{1}{n}})$

which provides the scaling of the drag force for $Bi \ll 1$ (see Hewitt & Balmforth (2018); illustrated for $n = 2$ in figure 2c).

For higher yield stress $Bi \gg 1$ and except over a narrow window of angles of motion with $\delta \ll 1$, the force components converge to $n-$independent values with $(F_x, F_z) \propto Bi$ (see figure 2c). These values correspond to the perfectly plastic limit of the problem in which the viscous stresses operate only in thin viscoplastic boundary layers (Balmforth *et al.* 2017) to adjust the solution and ensure no slip, without consequence on the net drag. The perfectly plastic deformation outside these boundary layers span distances of order of the cylinder radius. Importantly, in this plastic limit the two force components F_x and F_z remain comparable. Further details of these plastic solutions can be found in Appendix A.3 and figure 8.

However, as the cylinder approaches axial motion ($\delta \to 0$) there is a narrow window of angles $\delta \ll 1$ across which the transverse force F_x drops to zero, as it must on symmetry grounds ($F_x(\delta = 0, n, Bi) = 0$). The abrupt decrease in F_x arises without change in the axial force F_z, and so the force angle δ_f drops from $O(1)$ to zero across this window (see figure 2a). The width of this 'reorientation' window decreases with increasing Bi, and we previously showed that for a Bingham fluid ($n = 1$) the width of the window is $\delta = O(Bi^{-1})$ (Hewitt & Balmforth 2018). However, as illustrated in figure 2(a), the window is narrower for smaller n and wider for larger n. More specifically, we show in Appendix A.2 that the narrow window for force reorientation for $n \neq 1$ is instead given by $\delta = O(Bi^{-2/(n+1)})$, with

$$F_x \sim -\alpha_n \pi Bi^{\frac{n+3}{n+1}} \delta \qquad \& \qquad F_z \sim -2\pi Bi, \tag{2.6}$$

where

$$\alpha_n = \frac{(2n+1)^2(3n+1)}{\left[n^2(n+1)^{3n+1}\right]^{\frac{1}{n+1}}}, \tag{2.7}$$

(see Appendix A.2). The chief consequence of the narrow reorientation window for large Bi is that the direction of the induced force (δ_f) is highly sensitive to the direction of motion (δ) when this is shifted only slightly off-axis. Equivalently, substantial sideways forces can only be avoided if the translation of the cylinder is very closely aligned to its axis. As we will find below, this narrow reorientation window, and indeed the plastic flow solution for larger δ, have important consequences for slender locomotion through a viscoplastic material.

2.2. *Superposition*

We now return to the original $(X, Z)-$coordinate system and calculate the net forces induced by the swimming motion. Before entering into the details, we first move into the frame of the wave (in which the motion is independent of time) and remove the dimensions from the problem by scaling lengths (*i.e.* X, Z and $\mathcal{X}$) with the wavelength λ, speeds with the wavespeed c and stresses with $K(c/\mathcal{R})^n$. The swimmer is then periodic over a translating coordinate $0 \leqslant \zeta = Z + ct/\lambda \leqslant 1$; the centreline lies along $X = \mathcal{X}(\zeta)$, and a more natural Bingham number for the swimmer is

$$B_s = \frac{\tau_Y}{K(c/\mathcal{R})^n} \equiv V^n Bi, \tag{2.8}$$

where $V(\zeta) = \mathcal{U}/c$ is the dimensionless speed of each segment of the swimmer's body. That speed is not known a priori (as it depends on the locomotion speed of the swimmer) and must be found as part of the solution of the problem.

The constraint that the swimmer's centerline is perfectly inextensible demands that, in the frame of the wave, the body must move in the direction of the centerline at the constant speed,

$$Q = \int_{-\frac{1}{2}}^{\frac{1}{2}} \frac{\mathrm{d}\zeta}{\cos \Phi}, \tag{2.9}$$

which is the arc-length of the waveform relative to its undeformed length (Taylor 1952), where

$$\tan \Phi = \frac{\mathrm{d}\mathcal{X}}{\mathrm{d}\zeta} \tag{2.10}$$

denotes the local slope of the centerline (see figure 1). In a stationary (i.e. laboratory) frame, the swimmer's body therefore has velocity

$$(U, W) = Q \sin \Phi \hat{\mathbf{X}} + (Q \cos \Phi - 1 + W_s)\hat{\mathbf{Z}} \tag{2.11}$$

where W_s is the constant translation speed of the swimmer in the $\zeta-$direction; *i.e.* the dimensionless swimming speed (scaled by the wave speed; sometimes referred to as the 'wave efficiency'). Hence,

$$\begin{aligned} V \cos \delta &= Q - (1 - W_s) \cos \Phi, \\ V \sin \delta &= (1 - W_s) \sin \Phi, \end{aligned} \tag{2.12}$$

which allows determination of the speed

$$V(\zeta) = \sqrt{(W_s - 1)^2 + 2Q(W_s - 1)\cos \Phi + Q^2}, \tag{2.13}$$

and inclination

$$\tan \delta = -\frac{(W_s - 1)\sin \Phi}{(W_s - 1)\cos \Phi + Q}, \tag{2.14}$$

of each segment of the swimmer's body.

Given the slender-body results for the associated force components (F_x, F_z), we may compute the net axial force on the swimmer:

$$\frac{\lambda K c^n}{\mathcal{R}^{n-1}} \int_{-\frac{1}{2}}^{\frac{1}{2}} V^n (F_z \cos \Phi - F_x \sin \Phi) \frac{\mathrm{d}\zeta}{\cos \Phi}. \tag{2.15}$$

For steady swimming, this net force must vanish and so the integral constraint

$$\int_{-\frac{1}{2}}^{\frac{1}{2}} V^n (F_z - F_x \tan \Phi)\, \mathrm{d}\zeta = 0, \tag{2.16}$$

determines the swimming speed W_s. Finally, the dimensionless net dissipation rate, which must equal the dimensionless power $\mathcal{P}$ expended by the swimmer, can also be computed as

$$\mathcal{P} = \int_{-\frac{1}{2}}^{\frac{1}{2}} V^n \left[V \cos \delta F_z + V \sin \delta F_x\right] \frac{\mathrm{d}\zeta}{\cos \Phi} = Q \int_{-\frac{1}{2}}^{\frac{1}{2}} \frac{V^n F_z}{\cos \Phi} \mathrm{d}\zeta. \tag{2.17}$$

Note that the specific waveform $\mathcal{X}$ of the swimmer only enters the problem through the definition of Φ in (2.10); *i.e.* the slope of the centreline. In other words, for a given waveform, the amplitude and wavelength of the swimming gait are only relevant in how they combine to set Φ, which must remain sufficiently shallow for the slender-body theory to be applicable. More specifically, the radius of curvature of the centreline (which is $O(a^{-1}\lambda)$) must remain much greater than the swimmer's radius $\mathcal{R}$. For the sample waveforms that we adopt, this restriction demands that the wave amplitude parameter a should not be too large (specifically, $a \ll \lambda/\mathcal{R}$); this is a condition that we informally ignore in presenting model solutions, but is important to keep in mind.

3. Results

Figure 3 displays numerical results exploiting the construction of §2 for a swimmer propelled by the sinusoidal waveform $\mathcal{X} = a \sin 2\pi\zeta$. As indicated by the comparison of panels (a–c), for $n = \frac{1}{2}$, 1 and 2, respectively, the results for different power-law exponents are qualitatively similar. More significant is the role of the yield stress, with an increase of B_s prompting a clear increase in locomotion speed towards the wave speed.

The associated power expenditure, or dissipation rate, is shown in figure 4. Naturally, this measure increases with B_s as the swimmer has to break the yield stress to move; however, after compensating for this effect the figure shows a progressive decrease in the scaled power $\mathcal{P}/B_s$ for larger yield stress. The power steadily increases with wave amplitude, and approaches different high-Bi limits for small and large a, as discussed below.

An impression of the yielded sheath around the swimmer is displayed in figure 5, which shows the yield surfaces predicted in certain cross-sections through the swimmer for a range of values for a and B_s, and a particular choice of the dimensionless wavelength $\lambda/\mathcal{R}$ (which does not affect the wave speed or power). Not surprisingly, the yielded region becomes more localized as B_s is increased. On the other hand, as long as B_s is not small, variations in the wave amplitude can result in yield surfaces that lie at similar distances from the swimmer even while the the swimming speed increases by almost an order of magnitude (compare, for example, figure 5(c) and (f)). However, for smaller B_s and larger a, self-intersections of the yield surfaces can arise (e.g. figure 5g); the implied overlap of the yielded regions occurs when the span of the flow domain is no longer much smaller than the wavelength of the swimming stroke, and thus suggests a break down of the validity of the assumptions upon which the slender-body theory is based.

The characteristics displayed by the numerical results in these figures motivate a discussion of a number of limits of the problem, which we discuss below.

3.1. *Newtonian limit*

When $n = 1$ and $Bi \ll 1$, the force components have the limits in (2.4), and the constraint (2.16) reduces to

$$W_s = 1 - Q \left[\int_{-\frac{1}{2}}^{\frac{1}{2}} (2 \tan^2 \Phi + 1) \cos \Phi \, \mathrm{d}\zeta \right]^{-1}. \tag{3.1}$$

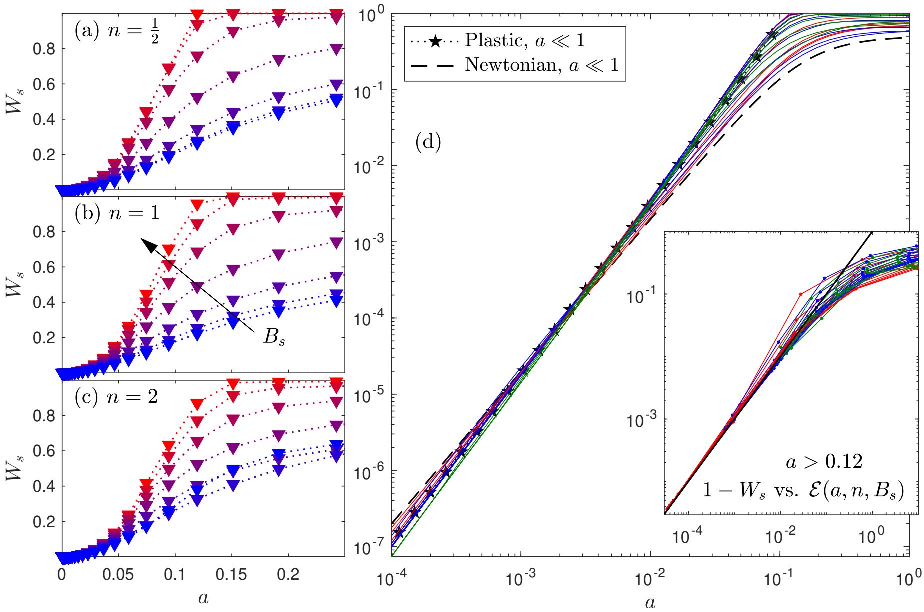

Figure 3: Locomotion speed W_s against wave amplitude a for a swimmer driven by sinusoidal waves in Herschel-Bulkley fluid with (a) $n = \frac{1}{2}$, (b) $n = 1$ and (c) $n = 2$. Examples with $B_s = 10^{-3}$, 10^{-1}, ... 10^3 are presented (colour coded by B_s, from blue to red). The data are replotted logarithmically over a wider range of a in (d), with $n = \frac{1}{2}$, 1 and 2 shown in red, blue and green (respectively). The dashed line shows the result for Newtonian fluid (§3.1; eq. (3.2)), and the low-amplitude, plastic solutions of §3.2 are shown by the stars. The inset in (d) shows the data for $a > 0.12$, replotted as $1 - W_s$ against the quantity $\mathcal{E}(a, n, B_s)$ defined in (3.17); the solid (black) line shows the prediction $1 - W_s = \mathcal{E}$ from §3.3.

For a sinsoidal wave profile, we then recover a result derived by Hancock:

$$W_s = 1 - \int_{-\frac{1}{2}}^{\frac{1}{2}} \sqrt{1 + 4\pi^2 a^2 \cos^2 2\pi\zeta}\, \mathrm{d}\zeta \left[\int_{-\frac{1}{2}}^{\frac{1}{2}} \frac{1 + 8\pi^2 a^2 \cos^2 2\pi\zeta}{\sqrt{1 + 4\pi^2 a^2 \cos^2 2\pi\zeta}} \mathrm{d}\zeta \right]^{-1}, \quad (3.2)$$

which gives $W_s \sim 2\pi^2 a^2$ for small a. For a more general swimming wave, if $\mathcal{X} = O(a)$ with $a \ll 1$ we set $\Phi = a\Phi_1 \sim a\mathcal{X}_1'$, $Q = 1 + a^2 Q_2 = 1 + \frac{1}{2}a^2 \int_0^1 \Phi_1^2 \mathrm{d}\zeta$ and $W_s = a^2 W_2$. Then,

$$W_2 \sim \int_{-\frac{1}{2}}^{\frac{1}{2}} \Phi_1^2 \mathrm{d}\zeta. \quad (3.3)$$

3.2. *Low-amplitude plastic swimming*

For low amplitudes, $(\mathcal{X}, \Phi) = O(a)$ with $a \ll 1$, we once more assume that $W_s = a^2 W_2$, which implies from (2.12)-(2.14) that $V = O(a)$ and $\tan\delta = O(a^{-1}) \gg 1$ everywhere except close to the extrema of the waveform. Near these extrema, where Φ becomes $O(a^2)$, we instead find that $V = O(a^2)$ and δ runs through the entire range $[-\frac{1}{2}\pi, \frac{1}{2}\pi]$. Because V is always small, the low-amplitude limit corresponds to $Bi = O(a^{-n}) \gg 1$ or larger, if B_s is fixed (see (2.8)). This implies that, provided B_s is non-zero, the relevant problem to consider for the force

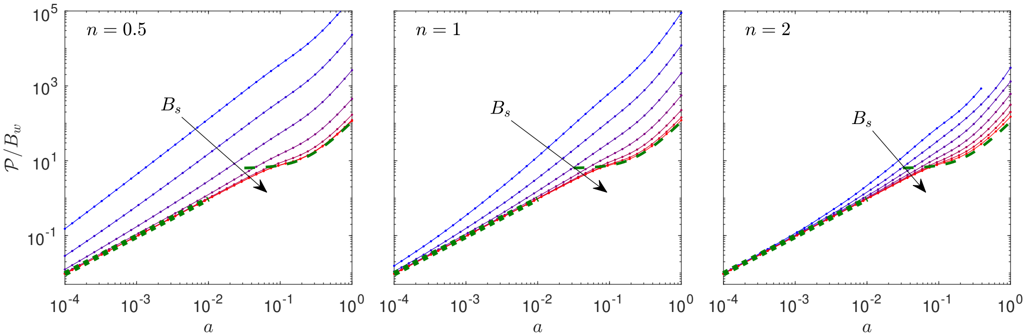

Figure 4: The scaled power $\mathcal{P}/B_s$ expended by a sinusoidal swimmer for $n = 0.5$, $n = 1$ and $n = 2$, as labelled, and different B_s between 10^{-3} and 10^3, coloured from blue to red. Two n-independent limiting values are also shown (green): low-amplitude plastic swimming (dotted) with $\mathcal{P}/B_s \sim 4f_x(\frac{1}{2}\pi)a \sim 16(\pi + 2\sqrt{2})a$, and plastic sliding for moderate a and $B_s \gg 1$ (dashed) with $\mathcal{P}/B_s \sim 2\pi Q^2$ ($\sim 32\pi a^2$ for large a with this gait).

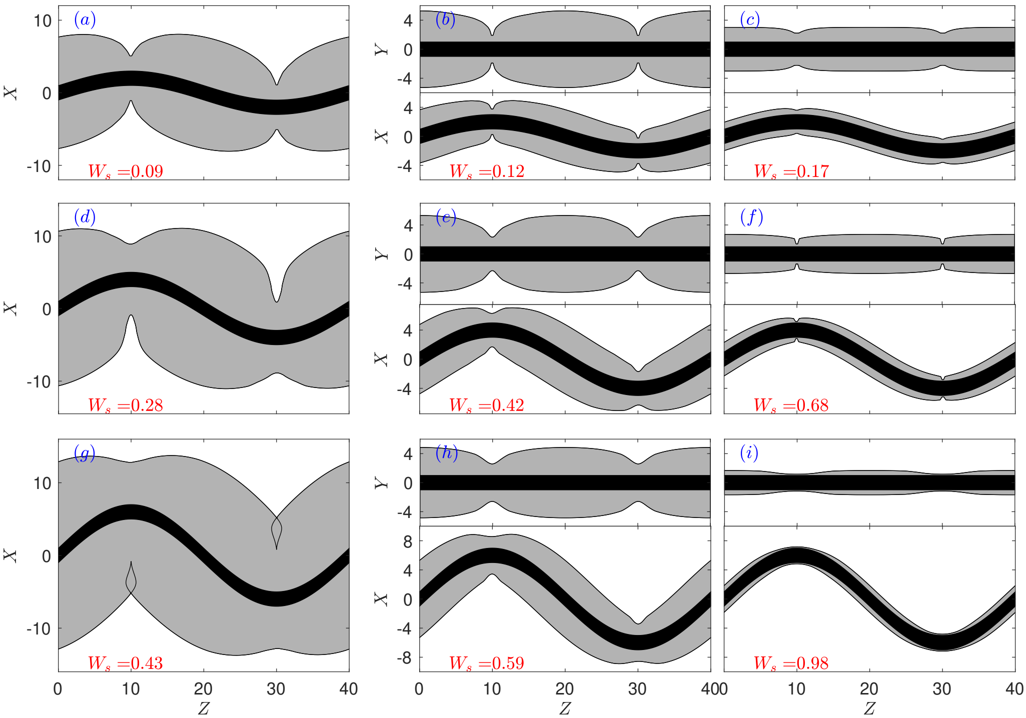

Figure 5: Yield surfaces (gray) around sinusoidal swimmer (black) with $n = 1$, wavelength $\lambda/\mathcal{R} = 40$, Bingham number $B_s = 0.1$ (left column), $B_s = 1$ (central column) and $B_s = 100$ (right column), and amplitude (scaled by the wavelength) $a = 0.05$ (upper row), $a = 0.1$ (middle row) and $a = 0.15$ (bottom row). The swimming speed is included in each panel (red). For the lowest B_s, only the plane of the wave is shown; higher B_s solutions also include the out-of-plane yield surfaces (upper plots in each panel).

components when $a \ll 1$ is the plastic limit $Bi \gg 1$, with δ not restricted to small values (*i.e.* beyond the reorientation window, which is considered below in §3.3 and Appendix A.2).

As discussed further in Appendix A.3, the force components in this plastic limit take the form

$$F_x(\delta, n, Bi) \sim -Bi f_x(|\delta|)\,\mathrm{sgn}(\delta) \qquad F_z(\delta, n, Bi) \sim -Bi f_z(|\delta|)\,\mathrm{sgn}(\cos\delta) \tag{3.4a, b}$$

for some functions f_x and f_z. These can be extrapolated from numerical results for $Bi \gg 1$, as plotted in figure 8 in the Appendix. The important details for this analysis are the limiting value $f_x(\frac{1}{2}\pi) \equiv 4(\pi + 2\sqrt{2})$, which can be extracted from the perfectly plastic solution in that limit (Randolph & Houlsby 1984), and the fact that a linear relationship

$$f_z \approx A(\tfrac{1}{2}\pi - |\delta|), \tag{3.5}$$

provides a very good fit to the data across the whole range of δ, with $A \approx 4.4$.

In view of (3.4), the constraint of vanishing drag (2.16) becomes

$$A \int_{-\frac{1}{2}}^{\frac{1}{2}} (\tfrac{1}{2}\pi - |\delta|)\mathrm{d}\zeta \sim a \int_{-\frac{1}{2}}^{\frac{1}{2}} f_x(|\delta|)|\mathcal{X}_1'|\mathrm{d}\zeta, \tag{3.6}$$

which is independent of n. Here, we have again introducted $\Phi = a\Phi_1 \sim a\mathcal{X}_1'$. The contributions to the integrals in (3.6) therefore arise from a "global" region, where

$$\Phi_1 = \mathcal{X}_1' = O(1) \quad (\Phi = O(a)), \quad \delta \sim \tfrac{1}{2}\pi\,\mathrm{sgn}(\Phi_1) - \frac{a}{\Phi_1}(Q_2 + \tfrac{1}{2}\Phi_1^2 + W_2), \tag{3.7}$$

and from "local" regions around the waveform's extrema, where

$$\Phi_1 = \mathcal{X}_1' = O(a) \quad (\Phi = O(a^2)), \quad \delta \sim \tan^{-1}\frac{\Phi_1}{a(Q_2 + W_2)}, \tag{3.8}$$

with $Q = 1 + a^2 Q_2$ and $W_s = a^2 W_2$ again, and we have assumed $Q_2 + W_2 > 0$. For symmetrical waveforms, $\mathcal{X}(\zeta) = -\mathcal{X}(-\zeta)$ and $\mathcal{X}(\zeta) = \mathcal{X}(\frac{1}{4} - \zeta)$, with extrema $\mathcal{X}(\pm\frac{1}{4}) = \pm 1$, the leading-order global contributions to the left and right-hand sides of (3.6) are

$$2aA + 4aA(Q_2 + W_2)\int_0^{\frac{1}{4}-\varepsilon} \frac{\mathrm{d}\zeta}{|\mathcal{X}_1'|} \qquad \text{and} \qquad 4af_x(\tfrac{1}{2}\pi) \tag{3.9}$$

respectively, where the splitting point ε is arbitrary but satisfies $a \ll \varepsilon \ll 1$. The left-hand side has two local contributions, each equal to

$$\frac{2aA(Q_2 + W_2)}{|\mathcal{X}_1''(\frac{1}{4})|}\int_0^Y (\tfrac{1}{2}\pi - \tan^{-1} y)\mathrm{d}y, \qquad Y = \frac{\varepsilon|\mathcal{X}_1''(\frac{1}{4})|}{a(Q_2 + W_2)}. \tag{3.10}$$

The integrals in (3.9) and (3.10) diverge logarithmically for $\varepsilon \to 0$. In writing the full constraint, we therefore reorganize accordingly to arrive at the implicit equation,

$$(Q_2 + W_2)\left\{J + \log\left[\frac{|\mathcal{X}_1''(\frac{1}{4})|}{a(Q_2 + W_2)}\right]\right\} \sim \frac{f_x(\frac{1}{2}\pi) - \frac{1}{2}A}{A}|\mathcal{X}_1''(\tfrac{1}{4})|, \tag{3.11}$$

with

$$J = \left[|\mathcal{X}_1''(\tfrac{1}{4})| \int_0^{\frac{1}{4}-\varepsilon} \frac{\mathrm{d}\zeta}{|\mathcal{X}_1'|} - \log \varepsilon^{-1} \right]_{\varepsilon \to 0} + 1. \tag{3.12}$$

For the sinusoidal waveform, $J \approx 1.24$, and the predictions from (3.11) are included in figure 3(c). The results are surprisingly close to the corresponding Newtonian prediction (§3.1), at least over the range of amplitudes and rheological parameters used in the plot.

Equation (3.11) implies the presence of a potentially non-asymptotic $\log a^{-1}$ term, which demands that $W_s \to 1 - Q < 0$ for sufficiently small a. That is, the swimmer must inevitably reverse direction at very low amplitudes. For the sinusoidal waveform, the other factors in (3.11) conspire to arrange the speed reversal to arise for $a < 10^{-7}$, far less that the range of amplitudes used in figure 3. Figure 6 shows results for different waveforms given either by the sawtooth-like profile,

$$\mathcal{X} = \sum_{j=1}^{16} \frac{(-1)^{j-1}}{8\pi^2(2j-1)^2} \sin[2\pi(2j-1)z], \tag{3.13}$$

or the smoothed square wave

$$\mathcal{X} = \frac{\tanh(\varsigma \sin 2\pi\zeta)}{\tanh \varsigma}, \tag{3.14}$$

where ς is a smoothing parameter. For the latter, the speed reversal is observed for higher amplitudes provided the wave is sufficiently sharp (*i.e.* ς large enough). The fact that such strokes lead to the body swimming backwards implies a far more significant rheological effect than noted for other complex fluids.

The dissipation rate associated with this low-amplitude plastic swimming can be computed from (2.17), and reduces to the left-hand side of (3.6), up to a factor of B_s, in this limit. Thus the dissipation is $\mathcal{P} \sim 4af_x(\frac{1}{2}\pi)B_s \sim 16(\pi + 2\sqrt{2})aB_s$, which, unlike the swimming speed, is independent of the swimming gait (see figure 4) and scales linearly with the swimming amplitude a.

3.3. *Plastic sliding or burrowing*

The numerical results in figure 3 indicate that W_s approaches the wave speed for sufficiently strong amplitudes and yield stresses. Our rationalization of this observation is that at such parameter settings, the swimmer is able to exploit the strong drag anisotropy for small δ that is created by the narrow reorientation window (discussed §2.1), in order to 'slide' through the medium without appreciable drift. That is, each segment of the swimmer travels in essentially its local axial direction, while the associated force on that segment can be directed at a wide range of angles δ_f. Suppose the swimmer is in this limit, with swimming speed $W_s = 1 - \epsilon$ and $\epsilon \ll 1$. Then,

$$V \sim Q - \epsilon \cos \Phi \qquad \& \qquad \delta \sim \tan^{-1} \frac{\epsilon \sin \Phi}{Q} = \frac{\epsilon}{Q} \sin \Phi + ... \tag{3.15}$$

Consequently,

$$V^n(F_x \sin \Phi - F_z \cos \Phi) \sim \pi B_s \left[2 \cos \Phi - \frac{\epsilon \alpha_n B_s^{2/(n+1)}}{Q^{(3n+1)/(n+1)}} \sin^2 \Phi \right], \tag{3.16}$$

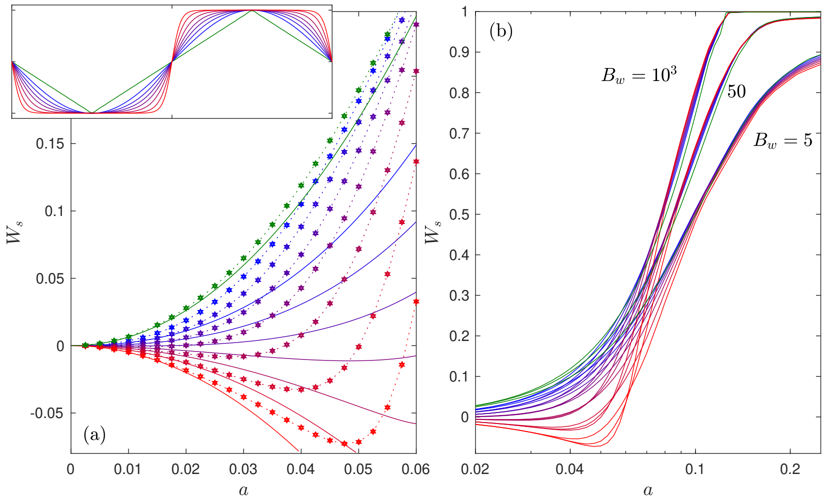

Figure 6: Swimming speed W_s against amplitude a for $n = 1$ and waveforms given by the sawtooth profile (3.13) (green) or smoothed square wave (3.14) with $\varsigma = 0.01$, 1, 1.5, 2, 2.75, 4 and 6 (from blue to red). In (a), the low-amplitude range is shown, with the solid lines showing the solution of (3.11) and the stars indicating numerical solutions, all with $B_s = 10^3$. In (b), higher amplitudes are shown, together with more numerical solutions with $B_s = 5$ (dashed) and 50 (solid). The inset in (a) displays the waveforms.

and the force-balance condition (2.16) demands that

$$\epsilon \sim \mathcal{E}(a, n, B_s) \equiv \frac{2Q^{(3n+1)/(n+1)} B_s^{-2/(n+1)}}{\alpha_n I}, \qquad I(a) = \int_0^1 \sin \Phi \tan \Phi \, \mathrm{d}\zeta. \quad (3.17)$$

The convergence of $1 - W_s$ to $\mathcal{E}(a, n, B_s)$ is confirmed by the numerical solutions, as displayed in the inset of figure 3(c).

We expect this theory to hold as long as δ lies within the narrow reorientation window, which requires $\alpha_n Bi^{2/(n+1)}\delta \lesssim \beta$, for some number β that we compute to be approximately 5 (see Appendix A.2 and figure 7). That is,

$$|\delta| \lesssim \frac{\beta}{\alpha_n} Bi^{-2/(n+1)} \qquad \Longrightarrow \qquad |\sin \Phi| \lesssim \tfrac{1}{2}\beta I(a) \approx \tfrac{5}{2} I(a), \qquad (3.18)$$

independent of n, at every point along the swimmer's body. Given the specific sinusoidal waveform in (2.1), this requirement reduces to $a \gtrsim 0.12$. Simultaneously, however, the swimming stroke should also fall within the plastic limit $Bi \gg 1$, which restricts the range of possible values of B_s; see the inset in figure 3(c), which demonstrates that $\mathcal{E}(a, n, B_s)$ must be small.

As discussed in Appendix A.2, the flow around the cylindrical body in the narrow reorientation window becomes restricted to a viscoplastic boundary layer. Consequently, in this form of burrowing locomotion the deformations are strongly localized, and the swimmer slides along a conduit that is only slightly bigger than its body. This feature is illustrated by the yield surfaces in the final column of figure 5.

Note that the condition in (3.18) is relatively insensitive to the waveform, being $a \lesssim 0.11 - 0.12$ for a variety of different profiles, including the sinusoid, sawtooth (3.13) and smoothed square waves (3.14). This feature can be seen in figure 6(b), where the speed data for $B_s = 50$ and 10^3 approach the limit $W_s \approx 1$ for such amplitudes, independently of the waveform.

The dissipation rate or power output in this limit (2.17) reduces to $\mathcal{P} \sim 2\pi Q^2 B_s$, as was shown in figure 4. The factor of $2\pi B_s$ follows from the need to exceed the yield stress around the unit radius of the swimmer in this limit; the dependence on Q, and thus on the swimming gait and amplitude, is simply geometric. While it is inevitable that the power must increase with B_s, because the swimmer needs to break the yield stress of the fluid to move, it is clear from the results in figure 4 that this plastic sliding motion is relatively efficient: the scaled power $\mathcal{P}/B_s$ is substantially lower than that for lower B_s, which presumably reflects the fact that the fluid must only be yielded in a narrow sheath around the swimmer in this limit.

4. Conclusion

In this paper, we have generalized a previous viscoplastic slender-body theory (Hewitt & Balmforth 2018) and applied it to the problem of locomotion in a complex fluid driven by a waving cylindrical filament. For low-amplitude waves, the stresses become dominated by the yield stress and the problem reduces to that for swimming through a perfectly plastic medium (more specifically, a rigid-plastic material with the von Mises yield condition, given our use of the Herschel-Bulkley viscoplastic constitutive law). A curious feature of this limit is that the swimming speed must become negative (i.e. the swimmer moves in the same direction as the wave) if the wave amplitude is sufficiently small relative to its wavelength. This phenomenon requires very small amplitudes and results in extremely small speeds when the swimmer employs a sinusoidal waveform, but is more pronounced with a square-wave-like swimming gait.

When wave amplitudes are not so small and for larger yield stresses, a key feature of viscoplastic slender-body flow comes into play: unless the motion is very closely directed along the axis of each cylindrical filament of the body, significant sideways forces arise; only in almost axial motion does the drag force become closely aligned with the direction of motion. In the locomotion problem, the appreciable anisotropy in the drag that is set up across the narrow angular 'reorientation' window allows the swimmer to 'burrow' through the medium by sliding along its axis at nearly the wave speed. An analysis of this limit of plastic sliding or burrowing indicates that the wave amplitude need not be particularly large (about one eighth of the wavelength), and this result is not particularly sensitive to the specific waveform of the swimmer.

Burrowing of this kind has been observed experimentally for various worms that naturally inhabit wet sediments or soils (Dorgan *et al.* 2013; Kudrolli & Ramirez 2019): these worms are found to travel along their axis at a swimming speed essentially equal to the wave speed (that is, a dimensionless wave speed or 'wave efficiency' of 1). Measurements on the polychaete worm *Armandia brevis* by Dorgan *et al.* (2013) revealed scaled amplitudes of $a \approx 0.18$, consistent with our theoretical prediction for being in the burrowing limit. While the relevance of plasticity in the ambient material to enable this form of locomotion has long been recognised (Dorgan *et al.* 2013; Dorgan 2015), the present study provides the first theoretical framework in which to describe such slender motion through a viscoplastic ambient.

The ability of a swimmer to exploit a sliding or burrowing mechanism to locomote emphasizes how the swimmer's body follows a conduit through the fluid. Although we have made no explicit inclusion of the ends of the slender body here, this style of locomotion clearly places extra focus on the dynamics of the head where the conduit is initiated. Opening mechanics of the conduits for worms in wet granular media and viscoelastic solids have previously been explored (Dorgan *et al.* 2005, 2007). Future biological application of the model presented here should pay closer attention to the dynamics at the head.

Appendix A. Analysis

A.1. *Formulation*

In this appendix we quote the dimensionless governing equations used Hewitt & Balmforth (2018), in which lengths are scaled by cylinder radius $\mathcal{R}$, velocities by the translation speed $\mathcal{U}$ of the cylinder and stresses by $K(\mathcal{U}/\mathcal{R})^n$. In the cylindrical polar coordinates system (r, θ, z) associated with the centreline,

$$\frac{1}{r}\frac{\partial}{\partial r}(ru) + \frac{1}{r}\frac{\partial v}{\partial \theta} = 0, \tag{A 1}$$

$$\frac{\partial p}{\partial r} = \frac{1}{r}\frac{\partial}{\partial r}(r\tau_{rr}) + \frac{1}{r}\frac{\partial}{\partial \theta}\tau_{r\theta} - \frac{\tau_{\theta\theta}}{r}, \qquad \frac{1}{r}\frac{\partial p}{\partial \theta} = \frac{1}{r^2}\frac{\partial}{\partial r}(r^2\tau_{r\theta}) + \frac{1}{r}\frac{\partial}{\partial \theta}\tau_{\theta\theta}, \tag{A 2a, b}$$

$$0 = \frac{1}{r}\frac{\partial}{\partial r}(r\tau_{rz}) + \frac{1}{r}\frac{\partial}{\partial \theta}\tau_{\theta z}, \tag{A 3}$$

where τ_{ij} is the deviatoric stress tensor, and subscripts indicate tensor components. The Herschel–Bulkley law relates the stress to the strain rate $\dot{\gamma}_{ij}$,

$$\tau_{ij} = \left(\dot{\gamma}^{n-1} + \frac{Bi}{\dot{\gamma}}\right)\dot{\gamma}_{ij} \qquad \text{for} \qquad \tau > Bi, \tag{A 4}$$

and $\dot{\gamma}_{ij} = 0$ otherwise, where the strain rate is related to the velocity field by

$$\{\dot{\gamma}_{ij}\} = \begin{pmatrix} 2u_r & v_r + (u_\theta - v)/r & w_r \\ v_r + (u_\theta - v)/r & 2(v_\theta + u)/r & w_\theta/r \\ w_r & w_\theta/r & 0 \end{pmatrix}, \tag{A 5}$$

subscripts of r and θ on the velocity components denote partial derivatives, and $\dot{\gamma} = \sqrt{\frac{1}{2}\sum_{ij}\gamma_{ij}\gamma_{ij}}$ and $\tau = \sqrt{\frac{1}{2}\sum_{ij}\tau_{ij}\tau_{ij}}$ denote the tensor second invariants.

With the scaling of the variables indicated in the main text, the cylinder translates in the $(x, z)-$plane with unit dimensionless speed at an angle δ to the $z-$axis (figure 1b). We therefore impose $(u, v, w) = (\cos\theta\sin\delta, -\sin\theta\sin\delta, \cos\delta)$ at $r = 1$. In the far field, the stresses must eventually fall below the yield stress and the fluid must plug up, such that $(u, v, w) \to (0, 0, 0)$.

On the surface of the cylinder ($r = 1$), the fluid exerts the force $(\tau_{\mathrm{rr}}, \tau_{\mathrm{r}\theta}, \tau_{\mathrm{rz}})|_{r=1}$, leading to a net drag per unit length of $\hat{\mathbf{x}}F_{\mathrm{x}} + \hat{\mathbf{z}}F_{\mathrm{z}}$, with

$$\begin{bmatrix} F_x \\ F_z \end{bmatrix} = \oint \begin{bmatrix} (-p + \tau_{\mathrm{rr}})\cos\theta - \tau_{\mathrm{r}\theta}\sin\theta \\ \tau_{\mathrm{rz}} \end{bmatrix}_{r=1} \mathrm{d}\theta = \oint \begin{bmatrix} 2\tau_{\mathrm{rr}}\cos\theta + (r\tau_{\mathrm{r}\theta})_r\sin\theta \\ \tau_{\mathrm{rz}} \end{bmatrix}_{r=1} \mathrm{d}\theta, \tag{A 6}$$

We solve these equations numerically using an Augmented Lagrangian finite-difference scheme, employing a Fourier transform in the azimuthal direction. This scheme differs from that used in Hewitt & Balmforth (2018) only by the inclusion of a non-linear viscosity to capture shear thinning or thickening for $n \neq 1$, and so is not described in detail here.

A.2. *Axial and nearly axial motion: force reorientation*

For purely axial motion, we have

$$r\tau_{rz} = -r_p Bi \qquad \& \qquad \tau_{rz} = -Bi - (-w_r)^n, \tag{A 7}$$

where $r = r_p$ denotes the (axisymmetrical) yield surface for which $\tau_{rz} = -Bi$ ($w_r < 0$), given that $w = 1$ on $r = 1$ and decreases to $w = 0$ with $w_r = 0$ at $r = r_p$. Hence,

$$w = 1 - \int_1^r \left[(r_p - r)\frac{Bi}{r}\right]^{\frac{1}{n}} \mathrm{d}r. \tag{A 8}$$

In the limit of a thin-gap limit, for $Bi \gg 1$, we have $r = 1 + Bi^{-1/(1+n)}\xi$ and

$$w_\xi \sim -(\xi_p - \xi)^{1/n}, \qquad w \sim \frac{n}{n+1}(\xi_p - \xi)^{(n+1)/n} \qquad \& \qquad \xi_p = \left(1 + \frac{1}{n}\right)^{\frac{n}{n+1}}. \tag{A 9}$$

where $\xi = \xi_p$ denotes the rescaled yield surface. Because the axial shear stress $\tau_{rz} \sim -Bi$ in this limit, the axial force is given by $F_z \sim -2\pi Bi$, corresponding to the perfectly plastic limit for a cylinder translating along its axis.

If, instead, the motion is nearly, but not exactly, aligned with the axis, and $Bi \gg 1$, the sideways translation is largely contained within $1 < r < r_p$ or $0 < \xi < \xi_p$, and the leading-order shear rate is $\dot{\gamma} \sim (\xi_p - \xi)^{1/n}$. The lateral force balances demand that

$$\frac{\partial p}{\partial \xi} \sim 0, \qquad \frac{\partial p}{\partial \theta} \sim Bi^{\frac{1}{n+1}}\frac{\partial \tau_{r\theta}}{\partial \xi} \sim Bi^{\frac{n+2}{n+1}}\frac{\partial}{\partial \xi}\left[\frac{v_\xi}{(\xi_p - \xi)^{1/n}}\right], \tag{A 10}$$

since

$$\tau_{r\theta} \sim \frac{Bi\ v_r}{|w_r|} \sim \frac{Bi\ v_\xi}{(\xi_p - \xi)^{1/n}}. \tag{A 11}$$

But $v = O(\delta)$ at $\xi = 0$ and $v(\xi_p, \theta) = 0$, and so

$$v \sim -\frac{n\xi(\xi_p - \xi)^{1+1/n}}{2n+1}Bi^{-\frac{n+2}{n+1}}\frac{\partial p}{\partial \theta}, \tag{A 12}$$

as long as $\delta \ll O(Bi^{-\frac{n+2}{n+1}}p)$, which turns out to be the case.

The continuity relation implies a radial velocity u given by

$$u_\xi \sim Bi^{-\frac{1}{n+1}}v_\theta \sim \frac{n\xi(\xi_p - \xi)^{1+1/n}}{2n+1}Bi^{-\frac{n+3}{n+1}}\frac{\partial^2 p}{\partial \theta^2}, \tag{A 13}$$

or

$$u \sim -\frac{n^2(\xi_p - \xi)^{2+1/n}[n\xi_p + (2n+1)\xi]}{(2n+1)^2(3n+1)}Bi^{-\frac{n+3}{n+1}}\frac{\partial^2 p}{\partial \theta^2}, \tag{A 14}$$

if $u = 0$ at $\xi = \xi_p$. But we also have that $u = \delta\cos\theta$ at $\xi = 0$, and so

$$p \sim \frac{(2n+1)^2(3n+1)}{n^3\xi_p^{3+1/n}}Bi^{\frac{n+3}{n+1}}\delta\cos\theta \tag{A 15}$$

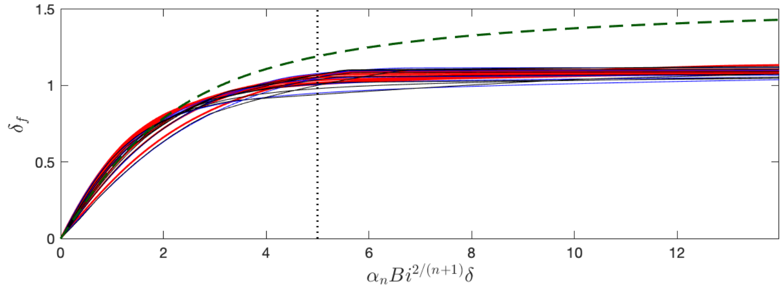

Figure 7: The force direction δ_f against $\alpha_n Bi^{\frac{2}{n+1}}\delta$ for $n=\frac{1}{2}$ (blue), $n=1$ (black) and $n=2$ (red), with $Bi=2^{j+n}$ and $j=3, 4, ..., 10$. The thick (green) dashed lines shows the prediction $\delta_f \sim \tan^{-1}(\frac{1}{2}\alpha_n Bi^{\frac{2}{n+1}}\delta)$. The vertical dotted line at $\alpha_n Bi^{\frac{2}{n+1}}\delta = 5$ roughly locates the window of strong force anisotropy.

Finally,

$$F_x \sim -\oint p\cos\theta \, \mathrm{d}\theta \sim -\alpha_n \pi Bi^{\frac{n+3}{n+1}}\delta, \tag{A 16}$$

where α_n is defined in (2.7). The transverse force therefore becomes dominated by the axial force $F_z = O(Bi)$ only when $\delta \ll O(Bi^{-2/(n+1)})$. The collapse of the force direction δ_F when plotted against $\alpha_n Bi^{\frac{2}{n+1}}\delta$ for different n (and large Bi) is illustrated in figure 7; also included is the prediction $\delta_f \sim \tan^{-1}(\frac{1}{2}\alpha_n Bi^{\frac{2}{n+1}}\delta)$ based on the preceding results.

A.3. *Plastic solutions outside the narrow window of force reorientation*

The nearly plastic solutions outside the narrow window where the force becomes reorientated are ilustrated in figure 8. These solutions are characterized by a region of almost plastic deformation surrounding the cylinder over distances of order the radius. The perfectly plastic flow is buffered by viscoplastic shear layers where the viscous stress remains important, and the two shear stress components τ_{nz} and τ_{sn} dominate the stress tensor. Here, s denotes the arc length along the centerline of the boundary layer and n is the transverse coordinate in the plane of the cylinder's cross-section. Of key importance is the shear layer against the cylinder, which transmits the fluid drag.

In the plastic limit, $Bi \to \infty$, the boundary layers become infinitely thin and feature jumps in tangential velocity. The corresponding plastic solution satisfies the slip conditions,

$$\begin{pmatrix}\tau_{nz}\\ \tau_{sn}\end{pmatrix} = -\frac{Bi}{\sqrt{V^2+W^2}}\begin{pmatrix}W\\ V\end{pmatrix}, \tag{A 17}$$

where V and W denote the jumps in the tangential velocity components, which can be extracted from a boundary-layer analysis like that used above. It does not seem possible to analytically find the limiting plastic solution for general δ (the method of sliplines, which proves useful in the purely two-dimensional flow problem, is not available here). For $\delta \to \frac{1}{2}\pi$, the transverse motion of the cylinder dominates the axial translation, which enters as a regular perturbation of the two-dimensional problem solved by Randolph & Houlsby (1984). In particular, one may calculate the transverse drag $f_x(\frac{1}{2}\pi)$ as quoted in §3.2. We also observe

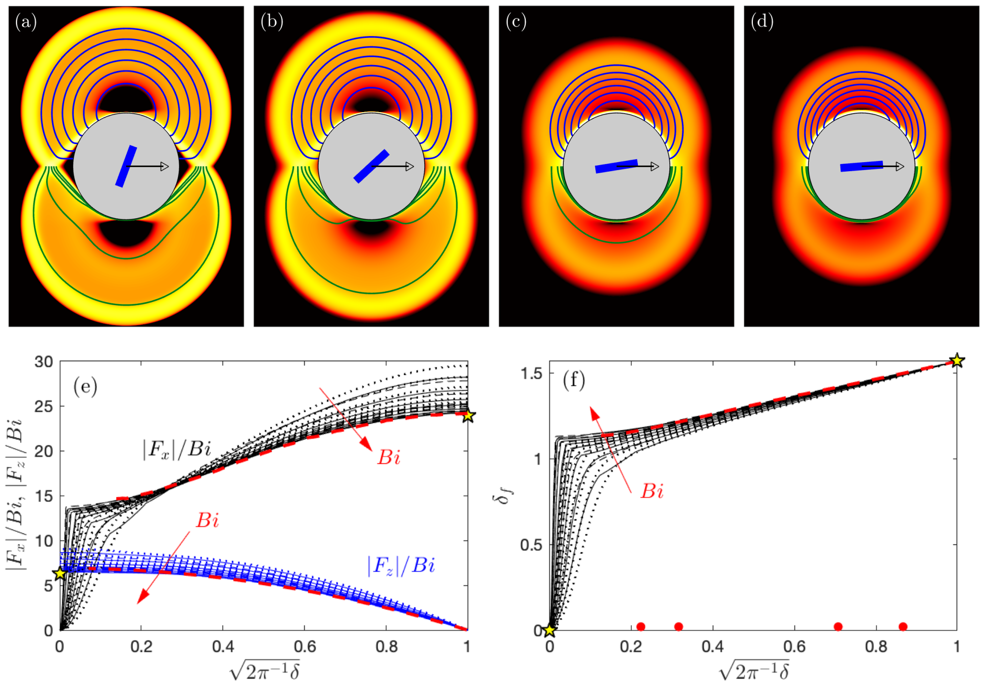

Figure 8: Numerical solutions showing the deformation rate invariant $\dot{\gamma}$ (as a density over the $(x, y)-$plane) and flow pattern (which has vertical symmetry; here showing streamlines of the planar velocity field $u\hat{\mathbf{x}} + v\hat{\mathbf{y}}$ in the upper half plane (blue); and contours of constant axial speed w in the lower half plane (green)) around a moving cylinder for $Bi = 1024$ and $n = 1$. The angle of inclination, shown pictorially in blue at the centre of each cylinder, is (a)–(d) $2\pi^{-1}\delta = [\frac{3}{4}, \frac{1}{2}, 0.1, 0.05]$. Panels (e) and (f) show the scaled drag components $(|F_x|, |F_z|)/Bi$ and direction δ_f against $\sqrt{2\pi^{-1}\delta}$ for $n = \frac{1}{2}$ (dashed), $n = 1$ (solid) and $n = 2$ (dotted), with $Bi = 2^{j+n}$ and $j = 3, 4, ..., 10$. The thick (red) dashed lines show the approximations $f_x(|\delta|)$ (extrapolated from the numerical results) and $f_z(|\delta|) = A(\frac{1}{2}\pi - |\delta|)$ with $A = 4.4$, as quoted in §3.2, and the stars indicate the analytical results for pure axial or transverse motion. The (red) points in (f) indicate the motion angles used for (a)-(d).

that the linear approximation (3.5) for f_z works well nearly all the way up to the reorientation window.

The limit $Bi \gg 1$ and $Bi^{-2/(n+1)} \ll \delta \ll 1$ is somewhat curious, as it corresponds to the sliding of a cylinder in the direction of its length through a perfectly plastic medium with an arbitrarily small (as long as Bi can be taken sufficiently large) but non-zero sideways translation. Associated with this motion is a finite transverse drag (the force angle approaches a value close to $\frac{1}{3}\pi$) and a flow pattern like that in figure 8(d) (save for the viscoplastic boundary layers, which shrink to slip surfaces as $Bi \to \infty$). Of course, the transverse drag eventually declines, and the flow pattern is consumed by the boundary layer of the axial velocity, as the motion aligns with the axis within the reorientation window. However, this requires a viscous effect (*i.e.* finite Bi). The origin of this curious feature is in the perfectly plastic solution itself: for pure axial motion, there is no deformation of the fluid, with the translation of the cylinder permitted by slip along its surface. But sideways translation cannot be accommodated by this style of motion, no matter how small, which instead demands plastic deformation over a finite region.

REFERENCES

Balmforth, N.J., Craster, R.V., Hewitt, D.R., Hormozi, S. & Maleki, A. 2017 Viscoplastic boundary layers. *J. Fluid Mech.* **813**, 929–954.

Balmforth, NJ, Frigaard, IA & Ovarlez, G 2014 Yielding to stress: recent developments in viscoplastic fluid mechanics. *Annual Review of Fluid Mechanics* **46**, 121–146.

Chan, D., Balmforth, N. J. & Hosoi, A. 2005 Building a better snail: lubrication theory and adhesive locomotion. *Phys. Fluids* **17**, 113101.

Chhabra, Raj P, Rami, Kirti & Uhlherr, Peter HT 2001 Drag on cylinders in shear thinning viscoelastic liquids. *Chemical engineering science* **56** (6), 2221–2227.

Cox, RG 1970 The motion of long slender bodies in a viscous fluid part 1. general theory. *Journal of Fluid mechanics* **44** (4), 791–810.

Denny, M. W. 1980 The role of gastropod mucus in locomotion. *Nature* **285**, 160–161.

Denny, M. W. 1981 A quantitative model for the adhesive locomotion of the terrestrial slug *ariolimax columbianus*. *J. Exper. Biol.* **91**, 195–217.

Dorgan, K.M. 2015 The biomechanics of burrowing and boring. *J. Exper. Biol.* **218**, 176–183.

Dorgan, KM, Arwade, SR & Jumars, PA 2007 Burrowing in marine muds by crack propagation: kinematics and forces. *Journal of Experimental Biology* **210** (23), 4198–4212.

Dorgan, K.M., Jumars, P.A., Johnson, B., Boudreau, B.P. & Landis, E. 2005 Burrowing mechanics: Burrow extension by crack propagation. *Nature* **433**, 475.

Dorgan, KM, Law, CJ & Rouse, GW 2013 Meandering worms: mechanics of undulatory burrowing in muds. *Proceedings of the Royal Society B: Biological Sciences* **280** (1757), 20122948.

Gidmark, NJ, Strother, JA, Horton, JM, Summers, AP & Brainerd, EL 2011 Locomotory transition from water to sand and its effects on undulatory kinematics in sand lances (ammodytidae). *Journal of Experimental Biology* **214** (4), 657–664.

Hancock, G. J. 1953 The self-propulsion of microscopic organisms through liquids. *Proc. Royal Soc. A* **217**, 96–121.

Hewitt, D.R. & Balmforth, N.J. 2017 Taylor's swimming sheet in a yield-stress fluid. *J. Fluid Mech.* **828**, 33–56.

Hewitt, DR & Balmforth, NJ 2018 Viscoplastic slender-body theory. *Journal of Fluid Mechanics* **856**, 870–897.

Hosoi, A.E. & Goldman, D.I. 2015 Beneath our feet: strategies for locomotion in granular media. *Ann. Rev. Fluid Mech.* **47**, 431–453.

Juarez, Gabriel, Lu, Kevin, Sznitman, Josue & Arratia, Paulo E 2010 Motility of small nematodes in wet granular media. *EPL (Europhysics Letters)* **92** (4), 44002.

Jung, Sunghwan 2010 Caenorhabditis elegans swimming in a saturated particulate system. *Physics of Fluids* **22** (3), 031903.

Keller, J. B. & Rubinow, S. I. 1976 Slender-body theory for slow viscous flow. *J. Fluid Mech.* **75** (4), 705–714.

Kudrolli, Arshad & Ramirez, Bernny 2019 Burrowing dynamics of aquatic worms in soft sediments. *Proceedings of the National Academy of Sciences* **116** (51), 25569–25574.

Lauga, E. & Powers, T.R. 2009 The hydrodynamics of swimming microorganisms. *Rep. Progr. Phys.* **72** (9), 096601.

Li, G. & Ardekani, A.M. 2015 Undulatory swimming in non-Newtonian fluids. *J. Fluid Mech.* **784**, R4.

Lighthill, Sir James. 1975 *Mathematical Biofluiddynamics*. SIAM.

Maladen, R.D., Ding, Y. & Goldman, D.I. 2009 Undulatory swimming in Sand: Subsurface Locomotion of the Sandfish Lizard. *Science* **325**, 314–318.

Pegler, S.S. & Balmforth, N.J. 2013 Locomotion over a viscoplastic film. *J. Fluid Mech.* **727**, 1–29.

Prager, W. & Hodge, P. G. 1951 *Theory of perfectly plastic solids*. Wiley.

Randolph, M.F. & Houlsby, G.T. 1984 The limiting pressure on a circular pile loaded laterally in cohesive soil. *Géotechnique* **34**, 613–623.

Riley, Emily E & Lauga, Eric 2017 Empirical resistive-force theory for slender biological filaments in shear-thinning fluids. *Physical Review E* **95** (6), 062416.

Supekar, R, Hewitt, DR & Balmforth, NJ 2020 Translating and squirming cylinders in a viscoplastic fluid. *Journal of Fluid Mechanics* **882**.

Tanner, RI 1993 Stokes paradox for power-law flow around a cylinder. *Journal of non-newtonian fluid mechanics* **50** (2-3), 217–224.

Taylor, G. I. 1952 The action of waving cylindrical tails in propelling microscopic organisms. *Proc. Royal Soc. A* **211**, 225–239.

Vélez-Cordero, J.R. & Lauga, E. 2013 Waving transport and propulsion in a generalized Newtonian fluid. *J. Non-Newtonian Fluid Mech.* **199**, 37–50.

Zhang, Tingnan & Goldman, Daniel I 2014 The effectiveness of resistive force theory in granular locomotion. *Physics of Fluids* **26** (10), 101308.